



Development of double-layer metamaterial with high effective medium ratio values for S- and C-band applications

Rasheduzzaman Sifat^a, Mohammad Rashed Iqbal Faruque^{a,*},
Tayaallen Ramachandran^a, Mardina Abdullah^a, Mohammad Tariquul Islam^b, K.S. Al-Mugren^c

^a Space Science Center (ANGKASA), Universiti Kebangsaan Malaysia, 43600 UKM, Bangi, Selangor, Malaysia

^b Department of Electrical, Electronic & Systems Engineering, Universiti Kebangsaan Malaysia, Bangi 43600 UKM, Bangi, Selangor D. E., Malaysia

^c Physics Department, Science College, Princess Nourah Bint Abdulrahman University, 84428, Ri-yadh 11671, Saudi Arabia

ARTICLE INFO

Keywords:

Double negative metamaterial
Split ring resonator
Electromagnetism
EMR
ASR application
Satellite application

ABSTRACT

This study introduces a compact double negative metamaterial (DNM) composed of three split rings connected slab resonator (TSRCSR) based double-layer design with a high 13.9 EMR (effective medium ratio) value. A double-layer patch is introduced to achieve the novel double negative properties, including negative behaviours of effective medium parameters, including refractive index, permittivity, and permeability with a high effective medium ratio for the miniaturised size of the introduced unconventional material that is highly suitable for microwave S and C band covering applications. The popular low-loss Rogers RT5880 (thickness 1.575 mm) substrate and copper resonator materials are utilized to develop the metamaterial unit cell that offers triple resonance between frequencies from 1 to 8 GHz. Therefore, the proposed metamaterial exhibits resonance peaks at 2.75, 5.2, and 6.3 GHz, suitable for radar, communication satellite, and long-distance telecommunication applications, respectively. The commercially available simulator known as Computer Simulation Technology (CST) is adopted to develop and simulate the $8 \times 8 \text{ mm}^2$ metamaterial design. The simulation results of the introduced TSRCSR design structure were verified by adopting the Ansys High-Frequency Structure Simulator (HFSS). Furthermore, it was then proved with the help of equivalent circuit model findings gained from the Advanced Design Structure (ADS) software. On the other hand, the analytical results were further validated by measuring the TSRCSR design utilizing a Vector Network Analyzer (VNA). These analyses become one of the novelties of this work, where the compact TSRCSR metamaterial successfully gained small discrepancies in transmission coefficient values when compared to both analytical and measurement results. The proposed metamaterial is highly suggested for communication devices for its extensive effective characteristics and compactness.

1. Introduction

Metamaterial embarks on its microwave man-made adventure by creating synthetic dielectric structures for controlling electromagnetic waves. Periodic metals on dielectric are known to have unique electromagnetic characteristics [1]. One such composite

* Corresponding author.

E-mail address: rashed@ukm.edu.my (M.R.I. Faruque).

<https://doi.org/10.1016/j.heliyon.2023.e23851>

Received 1 September 2023; Received in revised form 2 December 2023; Accepted 13 December 2023

Available online 18 December 2023

2405-8440/© 2023 The Author(s). Published by Elsevier Ltd. This is an open access article under the CC BY-NC-ND license (<http://creativecommons.org/licenses/by-nc-nd/4.0/>).

material is left-handed, and it exhibits negative behaviours of magnetic permeability and electric permittivity [2] at obtained frequency peaks. These uncommon electromagnetic properties of metamaterial were initially proposed by Veselago in 1968. Metamaterials also can exhibit either single negative permittivity or single negative permeability. The material found in nature does not have this characteristic. According to the specification, a metamaterial is a composite medium consisting of continuous wires and a periodic array of interspaced conducting nonmagnetic split ring resonators. In 1999, Pendry et al. [3] proved the combinations of split ring resonators and metallic wires may exhibit a below-zero refraction index at a specific frequency. Since 2005, the definition of metamaterial has expanded to include a configuration of synthetic structural components to provide unique and advantageous electromagnetic properties [4]. In 2010, synthetic medium that is organised on a scale smaller than the external wavelength influences had seen the most use of metamaterial [5]. In 2015, metamaterials were introduced as a manmade medium providing electromagnetic properties on demand [6]. Metamaterials are frequently recognized as constructed material for novel wave phenomena as the field advances quickly across electromagnetics today. Numerous prospects can be presented to new study areas by optimizing the metamaterial, such as absorber [7,8], antenna [9], gain enhancement [10], microwave application device - Wi-Fi, GPS [11,12], super-resolution [13–15], cloaking [16], radar cross-section (RCS) [17], reduction of specific absorption rate (SAR) [18], sensor [19], filter [20], perfect tunneling [21], radar and satellite [22,23], information metamaterial [24], terahertz metamaterial [25,26]. It's important to design the ideal system in several application sectors to obtain improved functioning with greater unit miniaturization and data measuring capability. Effective medium ratio (EMR) provides the establishment of an effective and compact designed structure where higher EMR can be achieved throughout the metamaterial development process.

The recent investigations on metamaterial covering the frequency band S, C, or both with their EMR are compared to better understand this investigation. For instance, Faruque et al. [27] developed a two C-shaped metamaterial design covering the S-, C-, and X-bands in 2017. The dimension of the device unit cell was $12 \times 12 \text{ mm}^2$ with an EMR of 7.42. Marathe et al. [28] achieved a miniaturised unconventional material unit cell in the same year. The size of the device was $6 \times 6 \text{ mm}^2$, and the achieved EMR was 11.5. The lower frequency was found at 4.3 GHz under the C-band. In 2019, a double L-shaped metamaterial [29] was introduced with a $10 \times 10 \text{ mm}^2$ unit cell structure, and the achieved EMR was 3.9, lower than the previously investigated design. The following year, in 2020, an inverse-epsilon-shaped metamaterial [30] with the same dimension of $10 \times 10 \text{ mm}^2$ was developed. The achieved EMR was

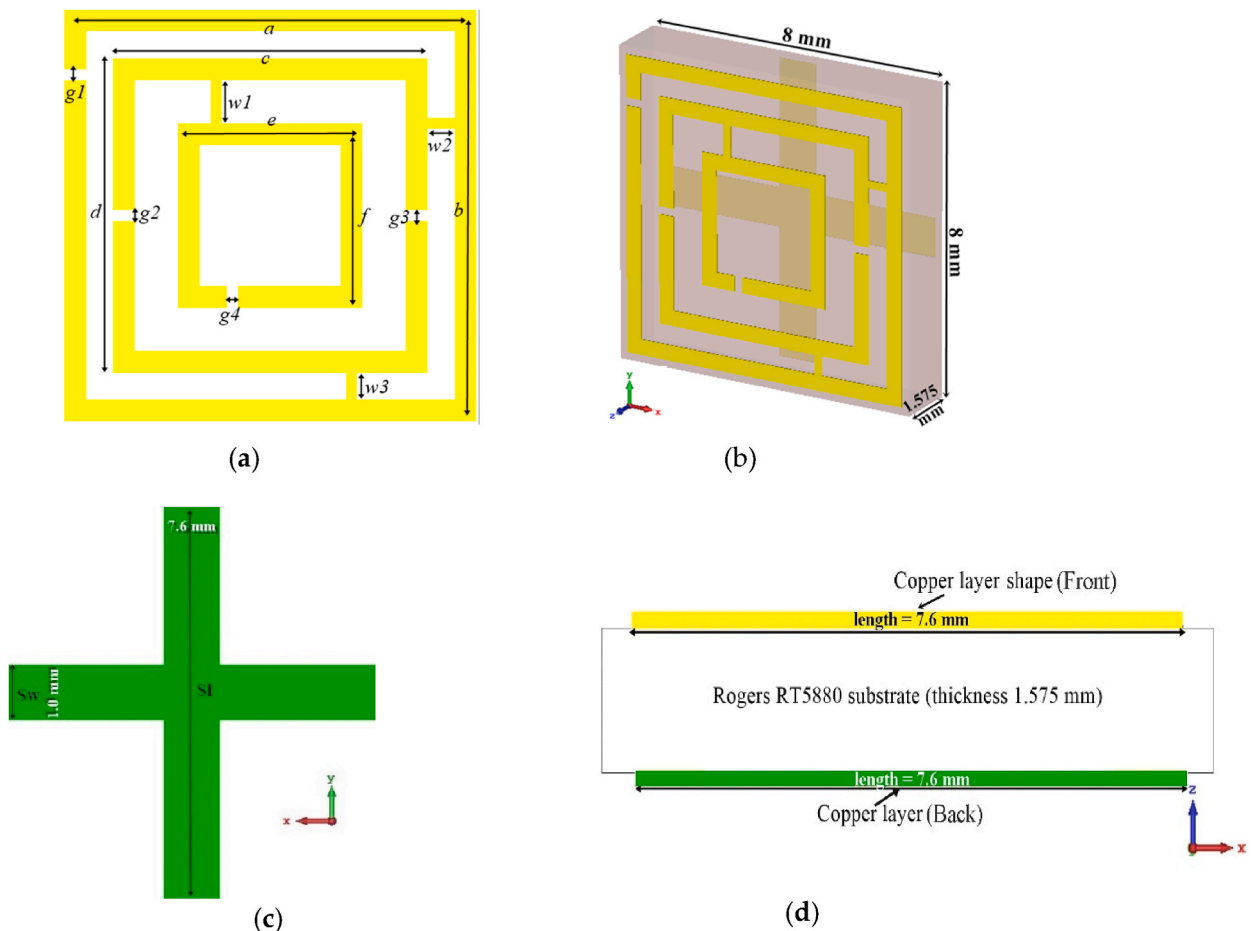


Fig. 1. TSRCRSR structure view from: (a) front; (b) perspective; (c) back; (d) coppers and substrate layer.

12.61 instead of having the same dimension as the previously discussed unit cell. The lowest frequency peak was observed at 2.38 GHz, exhibiting the design efficiency. Sifat et al. [31] established a novel structure with a dimension of $8 \times 8 \text{ mm}^2$ in the same year, and the achieved EMR was 12.78. The lowest resonance peak was found at 2.93. It is challenging to achieve a lower resonance on a compact-sized device through the design process.

This study presents three split rings connected slab resonator (TSRCSR) based double negative and layer metamaterial for S- and C-band communication fields. The previously discussed investigations were utilized for different application areas. The proposed metamaterial with the unique design structure evolving the latest technologies with simulation software and advanced methods are utilized to further optimize the outcome of the introduced metamaterial. The size, extraordinary characteristics, introduced split rings, application fields, and covering bands, including multiple resonances of the metamaterial design, need to be considered for its novel design. To achieve specific resonant frequencies or responses, metamaterial design itself is a very complex task. A rectangular ring resonator offers a high degree of design flexibility. Their dimension can be easily tailored to achieve certain resonance frequencies. The connecting slabs between the ring resonator act as a crucial part of achieving the specific response. In addition to miniaturised metamaterial with the dimension of $0.0733 \lambda \times 0.0733 \lambda$ covers triple resonances at 2.75, 5.21, and 6.28 GHz, correspondingly for WLAN and Radar communication applications at three resonance coverage, a TSRCSR-based metamaterial is developed. It has a bandwidth of 360 MHz (6.04–6.4 GHz) under -10 dB at resonance peak 6.3 GHz. Compared with the previously developed metamaterials at desired resonances, the proposed structure recorded a high EMR of 13.9, proving the balance of miniaturization and performance. The S-band, which has a resonance frequency of 2.75 GHz, is particularly well-liked for mobile network operators (MNO), ATC radars, and other applications, including mobile services and video streaming. The IEEE 802.11 specifications for WLAN allow for the usage of a peak point of 5.2 GHz. The unconventional material is constructed using the low-loss Rogers RT5880 substrate, which has a thickness of 1.575 mm. Furthermore, the finite integration method (FIT) is used to improve performance, and the CST software is appropriately utilized to develop the design and assessment. The main novelties of this work are the analyses of S21 results by adopting various analytical simulation software and performing measurement investigations to validate the results. Besides that, a significant challenge that arose during the compact metamaterial design construction process was solved by designing the SRR structure on the front and adding a unique shape at the back of the Rogers RT5880 substrate material. This allows, the limitation of gaining multiple resonance frequencies at the lower and higher bands at the same time. In a nutshell, the major objective of this work is to develop a compact miniaturised metamaterial with triple resonance frequencies despite keeping the parameters under the standard.

2. Metamaterial design

TSRCSR structure from front, perspective, back, and side views are demonstrated in Fig. 1 a to d. Meanwhile, the substrate size is $8 \times 8 \text{ mm}^2$ and it is the most popular and available low-loss substrate Rogers RT5880 with the loss tangent, dielectric constant, and thickness of 0.0009, 2.2, and 1.575 mm, accordingly. The copper layer is introduced on both sides of the substrate. The applied copper on the front layer is coated on the TSRCSR with a width of 0.2 mm and height of 0.035 mm where the copper with electrical conductivity of $5.8 \times 10^7 \text{ S/m}$. The copper back layer, which looks like an additional sign, is introduced to achieve the required resonances. The length and width of each stripe of the addition sign are 7.6 mm and 1 mm, respectively, and are placed vertically concerning each other. The substrate layer resembles a patty of the burger, whereas the two copper layers are the bun. The main design is involved the front copper layer and the back layer supports to gain the required results from the TSRCSR. The unique design was achieved by continuously changing the length, width, and position of the copper coating. The effects are also observed by utilizing the different substrate materials. The whole process is initially employed on the affordable software package known as the Computer Simulation Technology (CST) simulator where several models are utilized for simulation. The overall size of the suggested metamaterial is illustrated in Table 1. The modified results from the design process are illustrated in Fig. 2, where the scattering parameters are presented.

3. Methodology

Different models are utilized to investigate the metamaterial properties. Among the popular methods, we utilized the finite integration technique (FIT) in this study and the proposed design is performed and examined with simulation utilizing the CST simulation software. The reflection and transmission coefficients are computed by adopting the finite integration technique that also calculates the return loss as well as insertion loss. Through the waveguide port 1 and port 2, electromagnetic waves are generated and sent forward. The boundary requirements are met to direct the electromagnetic field toward the X and Y axes. The electromagnetic wave becomes polarized as it travels through the magnetic (H-field) and electric (E-field). Ideal electric and magnetic conductors are known to exist along the Y- and X-axes, accordingly. A perfect magnetic conductor (PMC) is used to model surfaces that perfectly reflect the magnetic field, much like a perfect electric conductor (PEC) perfectly reflects the electric field. When electromagnetic waves encounter a PMC boundary, the magnetic component of the wave is reflected with an inverted phase (180-degree phase shift) and passes through

Table 1
Unit cell metamaterial specifications.

Parameter	a & b	c & d	e & f	g1, g2, g3,g4	w1	w2, w3	sl	sw
Value (mm)	7.6	5.8	3.4	0.2	0.8	0.5	7.6	1

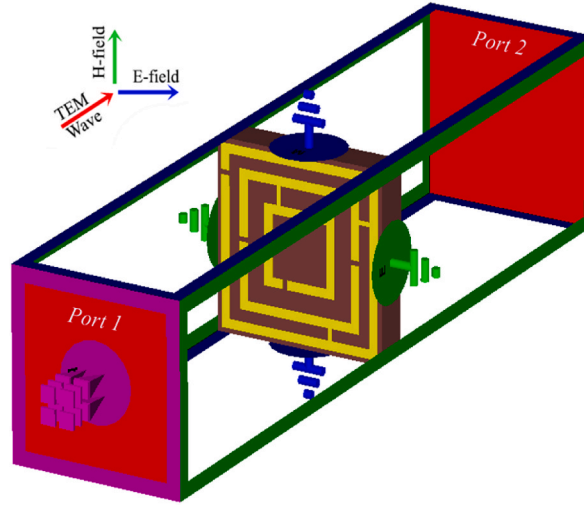


Fig. 2. Boundary condition setup for the TSRCRS unit cell design.

without reflection. Applying PMC boundary conditions along the y-axis is often used in simulations and designs of electromagnetic structures where a specific type of reflection behaviour is desired. For the simulation of free space, a frequency domain solver is employed. The proper LC circuit, in which the resonator strip serves as an inductor and the split gap as a capacitor, is implied by this metamaterial construction. The split gap and length of the metallic component are utilized to alter the capacitance and inductance. The microwave frequency range is used for the experiment from 1 to 8 GHz. Fig. 2 illustrates the boundary forms and the guided wave ports.

The Robust approach [32] is applied to derive the properties of ϵ , μ , and refractive index (η). Equations (1)–(7) are utilized to compute the parameters. The scattering parameters are considered from Equations (1) and (2).

$$S_{21} = \frac{(1 - R_{01}^2) e^{ink_0d}}{1 - R_{01}^2 e^{i2k_0d}} \tag{1}$$

$$S_{11} = \frac{R_{01} (1 - e^{i2nk_0d})}{1 - R_{01}^2 e^{i2nk_0d}} \tag{2}$$

where $R_{01} = \frac{z-1}{z+1}$. The metamaterial is found to be a passive medium. The refractive index along with the impedance's real and imaginary components are determined as described below.

$$z \text{ (real)} \geq 0 \tag{3}$$

$$\eta \text{ (imaginary)} \geq 0 \tag{4}$$

Equations (1) and (2) provide the impedance (z) and η .

$$z = \pm \sqrt{\frac{(1 + S_{11})^2 - S_{21}^2}{(1 - S_{11})^2 - S_{21}^2}} \tag{5}$$

$$e^{ink_0d} = X \pm i\sqrt{1 - X^2} \tag{6}$$

where $X = \frac{1}{2S_{21}(1 - S_{11}^2 + S_{21}^2)}$, refractive index (η) value can be obtained from Equation (6).

$$\eta = \frac{1}{k_0d} \{ [\ln(e^{ink_0d})]'' + 2m\pi - i[\ln(e^{ink_0d})]' \} \tag{7}$$

Here K_0 stands for the free space wave vector, and m stands for the inextricable link to the η index. The suggested structure's thickness is indicated by the notation d . The real part of η is involved by the logarithm function's subfunctions, but the imaginary part of η is only formally recognized. The actual fraction of effective medium parameters is calculated by adopting the usual extraction method which displays the resonance frequencies. The evaluation of effective parameters reveals the resonances. The relative permittivity (ϵ_r), relative permeability (μ_r), and relative refractive index (η_r) values are computed by adopting Equations (8–10), which are influenced by a series of gaps that are connected all at once to form a narrow gap in the band where ϵ_r and μ_r appear near the peak points [33].

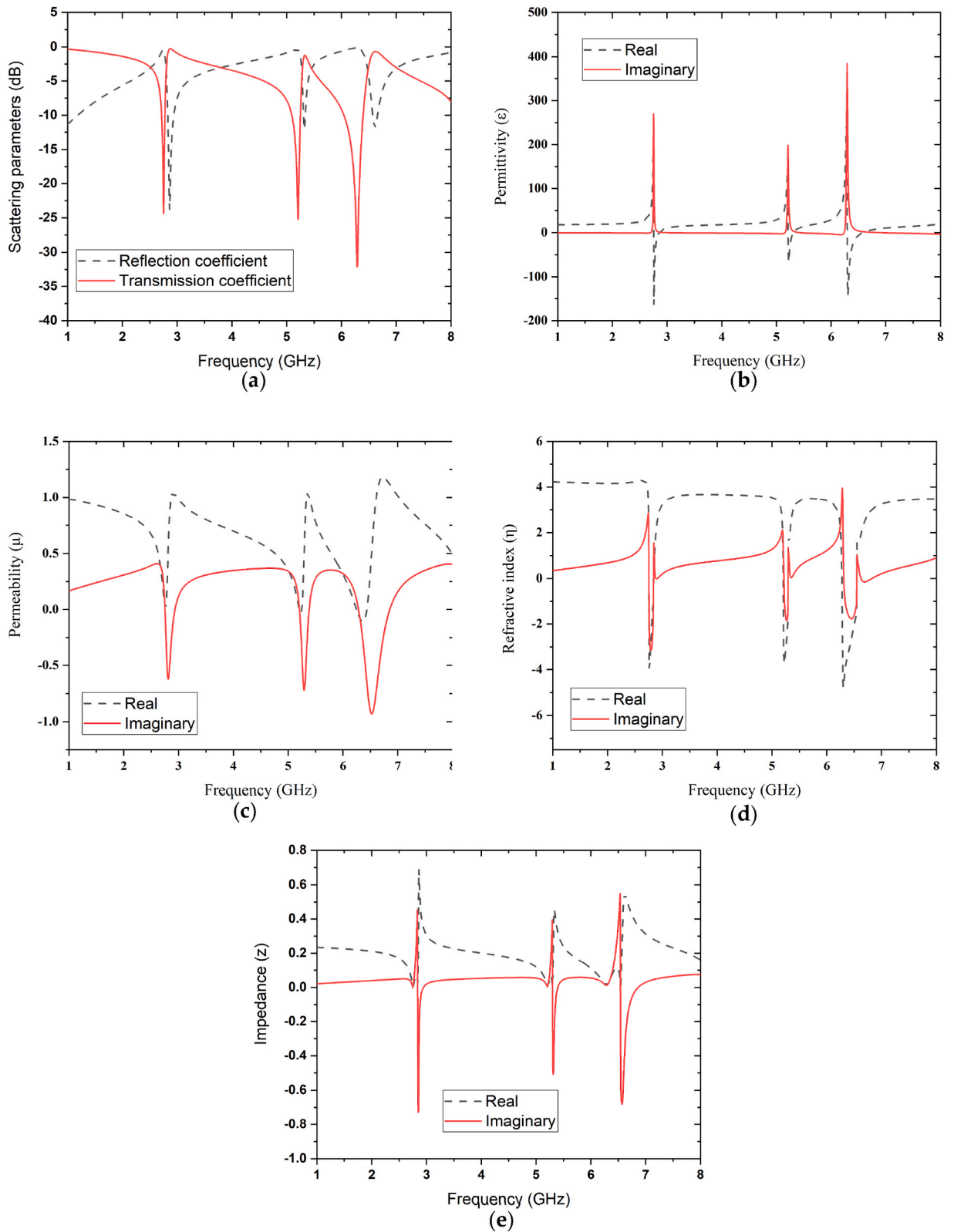


Fig. 3. Metamaterial unit cell properties: (a) S11 and S21; (b) effective relative permittivity; (c) effective relative permeability; (d) refractive index; (e) Impedance.

$$\epsilon_r = \frac{c}{j \pi f d} \times \frac{(1 - V_1)}{(1 + V_1)} \quad (8)$$

$$\mu_r = \frac{c}{j \pi f d} \times \frac{(1 - V_2)}{(1 + V_2)} \quad (9)$$

$$\eta_r = \frac{c}{j \pi f d} \times \sqrt{\frac{(S_{21} - 1)^2 - S_{11}^2}{(S_{21} + 1)^2 - S_{11}^2}} \quad (10)$$

The obtained resonance peaks from the suggested metamaterial design are 2.75, 5.2, and 6.3 GHz, according. Depending on the various design structures, the bandwidth may vary.

4. Results & discussion

The introduced TSRCSP properties are extracted and examined in this study. During this investigation, the mutual coupling effect is found. The EMR of the proposed TSRCSP design is also examined. It is also observed how the design responds in different-sized array structures as using the metamaterial structure as an array is obvious. These detailed results establish the correctness of the design. The numerical simulation process is utilized to investigate the frequency hopping properties of the device. The investigation results of recent related research works are also observed and discussed in the further section.

4.1. Unit cell property execution

The microwave computer simulator technology simulation S -parameters, ϵ , μ , η , z and S_{21} results on different simulator software are depicted in Fig. 3. The effective medium parameters are computed by using MATLAB. The graphs are created using the Origin Pro 2018 software which was the data retrieved by both CST and MATLAB software. Fig. 3 a displays the scattering parameters where the resonance frequencies of transmission begin at 2.75, 5.2, and 6.3 GHz. Fig. 3 b and c illustrate the imaginary and real parts of the ϵ_r and μ_r . The Rogers RT5880 substrate achieves optimal performance. The addition of the rear layer may have a significant influence on the relative permeability results, as opposed to the absence of the layer, which merely shows a negative permittivity and almost no permeability. The metamaterial's negative permeability is attained with the addition of the rear layer. Fig. 3 d presents the refractive index where it is observed that the triple resonance frequency has negative refractive index values which strongly establishes the metamaterial behaviour to refract the incident wave in the opposite direction compared to the traditional materials. Fig. 3 e displays the impedance which is a measurement of how a metamaterial interacts with electromagnetic waves. The impedance is closely related to the behaviour of ϵ_r and μ_r . For metamaterial with a negative refractive index, the impedance can also be negative.

4.2. Equivalent circuit

The commercially available computer simulation technology CST studio suite is utilized to retrieve the scattering parameters. The relative permittivity and permeability, refractive index are obtained from the S -parameters in MATLAB. The graphs on the Origin Pro 2018 software are drawn using the data produced by CST-MATLAB. The polarization properties along with the magnetic field, surface current and electric field are analyzed at 2.75 GHz, 5.2 GHz, and 6.3 GHz resonance frequencies. These electromagnetic field properties satisfy Maxwell's equation, and it is observed that the absence of the electric field occurs in the presence of the magnetic field including the current flow at a certain resonance frequency. The circuit model of the proposed design is constructed and analyzed to compare the results between the software simulation and hardware-based design as the unit cell acts as an LC circuit. There are several methods to modify the comparable circuit. The lumped equivalent circuit technique [34] is one method that accounts for microwave circuits, such as inductors, capacitors, and conductors. When creating the analogous circuit, the metal conductor is addressed using the inductor property. Each SRR functions like a circuit with inductors and capacitors. The split ring is a resonator that resonates at a certain frequency. The triple SRR and the metallic portion with a reflexive design serve as the foundation for the suggested construction. The following equations are used to achieve the inductance and capacitance of the metamaterial equivalent circuit design. Based on the transmission line principle, the whole inductance and capacitance of the proposed metamaterial are measured [35].

$$f = \frac{1}{2\pi\sqrt{LC}} \quad (11)$$

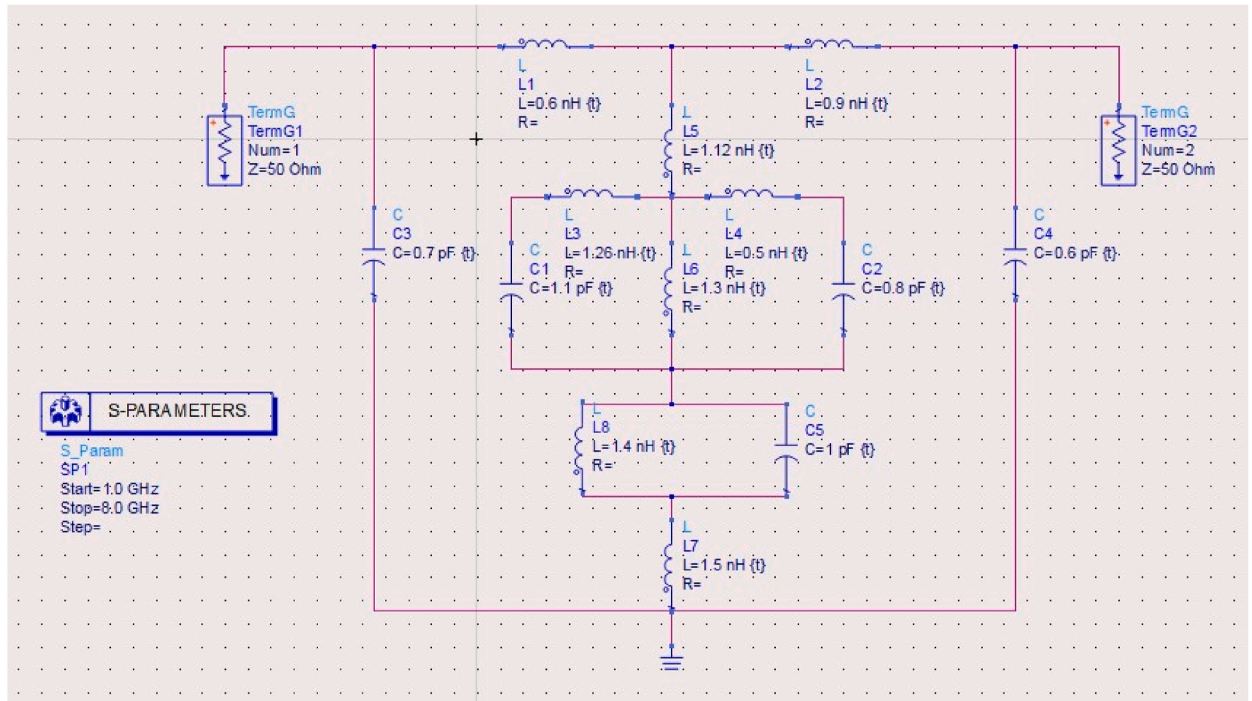
$$L = 0.01 \times \mu_0 \left\{ \frac{2(d+g+h)^2}{(2w+g+h)^2} + \frac{\sqrt{(2w+g+h)^2 + l^2}}{(d+g+h)} \right\} t \quad (12)$$

$$C = \epsilon_0 \left[\frac{2w+g+h}{2\pi(d+h)^2} \ln \left\{ \frac{2(d+g+h)}{(a-l)} \right\} \right] t \quad (13)$$

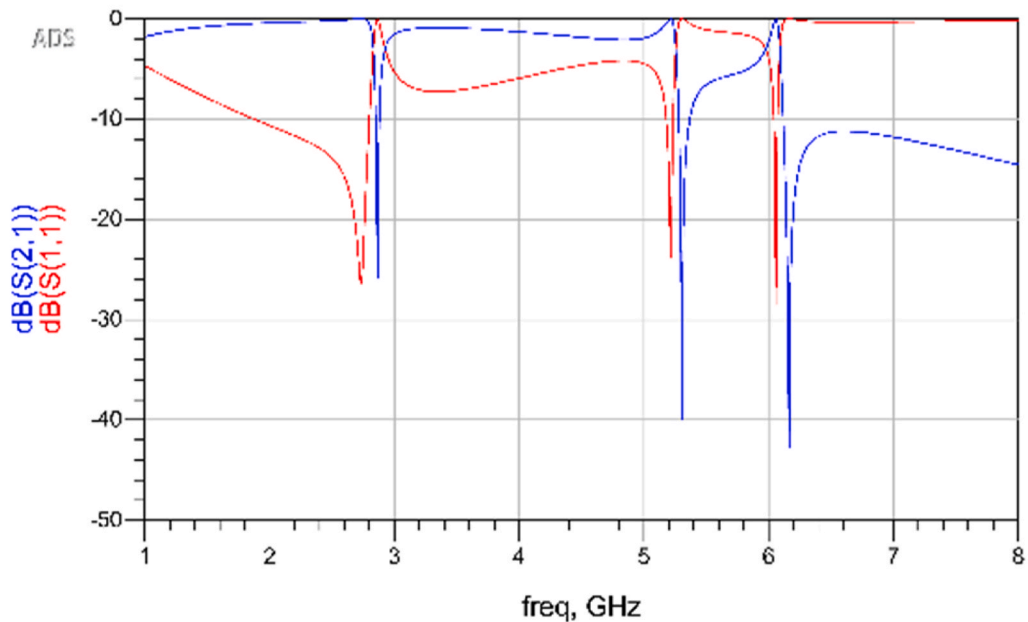
Here, $\epsilon_0 = 8.854 \times 10^{-12}$ F/m, $\mu_0 = 4\pi \times 10^{-7}$ H/m, thickness = h , split distance = d , resonator length = l , resonator width = w ,

copper resonator thickness = t , and ring split gap = g .

Fig. 4 a and b illustrate the circuit model of the metamaterial unit cell and the simulated scattering parameters of the equivalent circuit utilizing the ADS simulator software. In this circuit design, the split gaps were kept as capacitive effects, marked by the letters C1 to C5. Conversely, the inductive effects denoted as L1 through L8, were dependent upon how the strip lines were constructed. The corresponding circuit schematic contains series capacitance in each split gap because the proposed metamaterial is stimulated by the strength of an electric field. The S21 and S11 result from ADS software as shown in Fig. 4 b, which demonstrates small discrepancies in



(a)



(b)

Fig. 4. Advanced Design System ADS: (a) equivalent circuit model; (b) simulated scattering parameters.

resonant patterns. The values of the components are elaborated in Table 2.

4.3. Measurement result

The S21 outcomes were also gained during the measurement process to further validate the numerical result from CST, HFSS and ADS software. The proposed cells were built on a printed circuit board (PCB) for this experiment, as shown in Fig. 5a. The remaining copper material was removed throughout the production process based on the proposed TSRCRSR design. The constructed TSRCRSR design was then analyzed using measurement equipment known as the Agilent N5227A Vector Network Analyzer (VNA). With a frequency range of 10 MHz–67 GHz, this instrument is the highest-performing microwave network analyzer in the industry for testing passive and active devices. The VNA provides the best linear receivers and high-power sources for measuring scattering parameters with the best precision. Fig. 5b shows the proposed metamaterial cell positioned between two waveguide ports. For this measurement, two adapters were used: A-INFOMW WG to Coaxial adapter P/N: 187WCAS for S-band and A-INFOMW WG to adapter P/N: 137WCAS for C-band. To provide an accurate result, an Agilent N4694-60001 device is utilized to calibrate the VNA prior.

Fig. 5c demonstrates the S21 results obtained from the CST, HFSS, ADS simulation software and VNA measurement. Early discovery reveals that the proposed TSRCRSR design also manifests three resonance frequencies when conducting the measurement process. For instance, the TSRCRSR design successfully exhibits resonance frequencies with band gaps under -10 dB magnitude values at 2.20–2.90 GHz, 4.75–5.53 GHz, and 6.20–6.52 GHz, respectively. Meanwhile, the peak resonance points reach 2.67, 5.28, and 6.40 GHz with magnitude values of -15.91 , -23.82 , and -24.65 dB. Moreover, the comparison of the numerical and measured results demonstrates moderately small differences between them. Due to the highest discrepancy of 2.91% only recorded in the first resonance frequency, it can be neglected. Although the measurement findings exhibit highly satisfactory results with minimal variations, the inconsistencies were caused by several reasons. To begin, calibration mistakes may have an impact on the measurement result. The Agilent N4694-60001 electronic calibration (ECal) kit was typically used to provide precise and acceptable results by minimising ambient temperature impacts. Furthermore, this effect relates to drift mistakes induced by changes in performance after the calibration process has been completed. As a result of these temperature effects, incorrect results may be produced. As a result, a researcher can mitigate the impacts by keeping the temperature constant throughout the experiment. In other words, this measurement process requires a properly stable ventilation system and well-warmed equipment. Overall, the S21 results comparison of all the different simulation results such as CST (Computer Simulation Technology) studio suite, HFSS (High-Frequency Simulation Software), and ADS (Advanced Design System) revealed small discrepancies between them. The different methods and techniques are utilized to achieve the results through the simulation software where HFSS is based on the Finite element method (FEM) and CST is based on Finite integration in technique (FIT). Based on the different technologies, the achieved results are not overlapped with each other but it is noticeable to have the similarity in results.

4.4. EMR analysis

The EMR is a measurement of the compactness of the unit cell design. By dividing the wavelength attained at the lowest resonance frequency by the unit cell size, the EMR can be calculated. The efficacy of the device is shown once the EMR value is more than 4, either it can be a single negative or a double negative metamaterial. The following equation is used to calculate the EMR of the metamaterial [36].

$$EMR = \frac{\lambda}{D} \quad (14)$$

Here λ and D stand for wavelength and dimension, respectively. The comparison shows that the recommended structure owns the high EMR concerning its application sector.

4.5. E-field, H-field, surface current, and pointing vector

In this section, at 2.75 GHz, 5.2 GHz, and 6.3 GHz, electric field circulation is analyzed. The propagation constant ($|\gamma^2|$) of the metamaterial can be achieved by the determined resonance frequency, permittivity, permeability and conductivity through the Helmholtz equation [37].

$$|\gamma^2| = \omega\mu\sqrt{\sigma^2 + \omega^2\epsilon^2} \quad (15)$$

Here, γ is the propagation constant, ω = resonance frequency, ϵ = permittivity, μ = permeability and σ = conductivity. A linear

Table 2
Equivalent circuit model parameters and values.

Component	Value	Component	Value	Component	Value (pF)	Component	Value
C1	1.1 pF	C4	0.6 pF	L2	1.6 nH	L5	1.12 nF
C2	0.8 pF	C5	1 pF	L3	1.36 nH	L6	1.3 nF
C3	0.7 pF	L1, L7	1.5 nH,	L4	0.5 nH	L8	1.2 nH

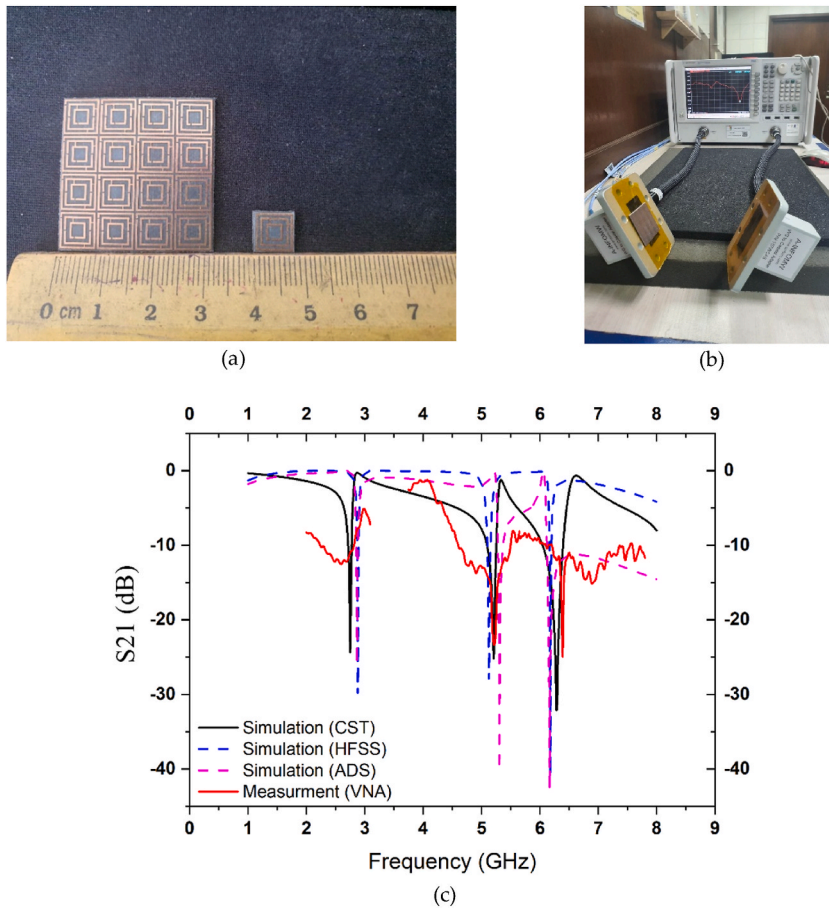


Fig. 5. Measurement of the proposed metamaterial: (a) Fabricated metamaterials; (b) VNA set-up; (c) S21 results of CST, HFSS, ADS simulation and measurement results from VNA.

homogeneous differential equation is utilized to integrate the components to elaborate the characteristics of the E-field distribution at a certain resonance frequency as shown in equation (16).

$$\left[\frac{d^2}{dz^2} - \gamma^2 \right] E_{xm}(z) = 0 \tag{16}$$

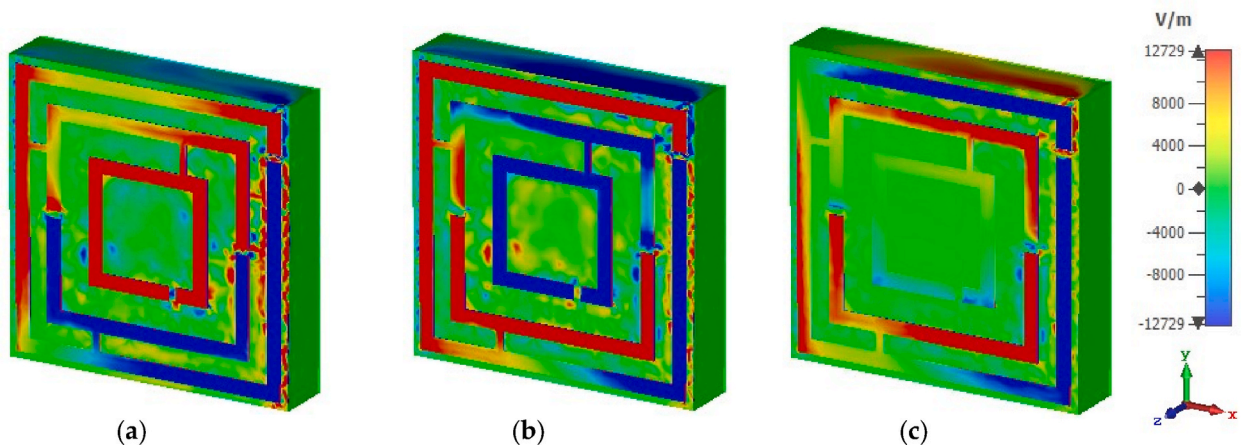


Fig. 6. Electric field (E-field) at the resonance frequency: (a) 2.75 GHz; (b) 5.2 GHz; and (c) 6.3 GHz.

The E-field distribution over the metallic structure is shown in Fig. 6 when the wave propagation through the z-axis is simulated. The inner fidget form region of the metamaterial unit cell also exhibits electric field characteristics. Additionally, the metamaterial unit cell's inner SRR and the top area of the middle and outer SRR also display a strong electric field at 2.75 GHz frequency. A strong electric field is produced and is equally shared. This design achieves notable outcomes for long-distance telecommunication communication applications; the bandwidth is measured below -10 dB and employs 2.75 GHz, 5.2 GHz, and 6.3 GHz as the resonance frequencies. These triple resonance frequencies are utilized to analyze the surface current distribution, magnetic field, and electric field, respectively. At 2.75 GHz frequency (Fig. 6a), the inner SRR and top regions of the middle and outer SRR of the metamaterial unit cell exhibit a high electric field. Additionally, a dispersed strong electric field is seen at 5.2 GHz (Fig. 6b) in the inner SRR and the left-bottom portion of the outer SRR. Furthermore, an active electric field with a resonance frequency of 6.3 GHz (Fig. 6c) can be detected in the top, left, and bottom portions of the outer SRR. Fig. 7 illustrates that the magnetic field is apparent in the structure's rest zones, where the electric field is not present. The criteria of Maxwell's equation are satisfied by these electromagnetic field properties. Fig. 8 depicts a significant surface current flow in these areas when a strong magnetic field is present. The proposed design's current concentration produces a considerable magnetic dipole across the outer SRR metallic component. The current flow is displayed in the areas where the magnetic field intensity is reached. Fig. 9 shows that the energy flux circulates the SRR at 2.75 GHz (Fig. 9a), which is consistent with strong centred resonance. For the resonance 5.2 GHz (Fig. 9 b), the energy flux is strong and propagates to the left side along the surface. Fig. 9(c) illustrates the comparatively weak energy fluxes that move around the SRR at the 6.3 GHz frequency.

5. Parametric study

5.1. Unit cell design process

Table 3 elaborates on the proposed metamaterial design parameters. The initial TSRCSSR metamaterial construction process is inaugurated with a single SRR on the substrate front layer. For instance, 'Design 1' was proposed with a metallic copper stripe of 0.4 mm wide, a split gap of 0.2 mm and a dimension of 7.6×7.6 mm². The thickness of this design layer is 0.035 mm. The achieved resonance frequency found from this design is 3.54 GHz which is under the C-band. On the other hand, another SRR is placed inside the first SRR with a length and width of 5.8 mm and 5.8 mm, respectively. This step is entitled 'Design 2', where the resonance peak is observed at 3.55 GHz and 4.45 GHz under the S- and C-bands. On the other hand, another SRR is introduced inside the second SRR with a width and length of 3.4 mm, accordingly, as shown in 'Design 3'. From this step, the design achieved the almost same resonance peaks near 3.55 GHz and 5.45 GHz under the same S- and C-band. However, in 'Design 4', a crucial step was adopted where the SRRs are connected by copper slabs with a width of 0.2 mm. The connected slabs dramatically turn the result into three peak points at 3.31, 3.54, and 7.18 GHz. These resonance peaks under S- and C-bands are found by the design process while the incident wave is induced on the metamaterial layers. According to Lenz's law, the connecting slabs work like inductors where the copper layer's conductive portion possesses both inject properties and magnetic energy. The split gap in an SRR works like an inductor, which is observed in 'Design 5' where several split gaps are introduced on the SRRs. It is also remarked that the shifted peak points under the S-band is seen at 2.75 GHz. The previously observed resonances are shifted to the lower resonance at 6.3 GHz from the resonance peaks and 7.18 GHz. Another layer is attached to the back of the substrate material with a copper coating initially established. The length and width of the two metallic slabs on this layer are 7.6 mm and 1 mm, respectively, and placed crossly, which looks like an additional sign '+'. This layer impacts the resonances and relative parameters of the design structure whenever the induced electromagnetic waves may occur in the mutual coupling between the SRRs and slabs.

From the proposed design of the TSRCSSR, we achieved negative permittivity (ϵ), negative permeability (μ) and negative refractive index (η). The observed characteristic of the developed design is described in the methodology section of this study. Different dielectric substrates were utilized to achieve the required results however the popular substrate Rogers RT5880 was finally utilized. Fig. 10

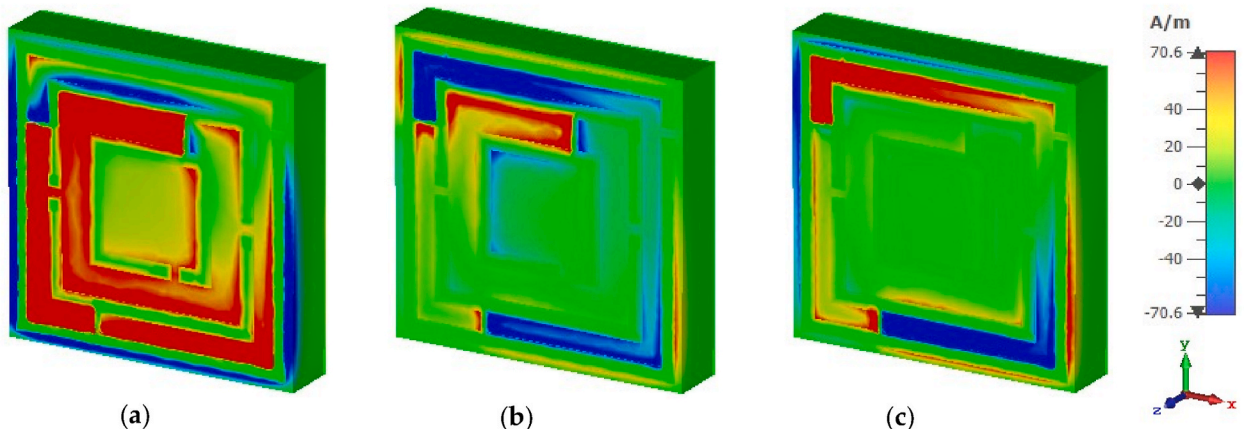


Fig. 7. Magnetic field (H-field) at resonance frequency: (a) 2.75 GHz; (b) 5.2 GHz; and (c) 6.3 GHz.

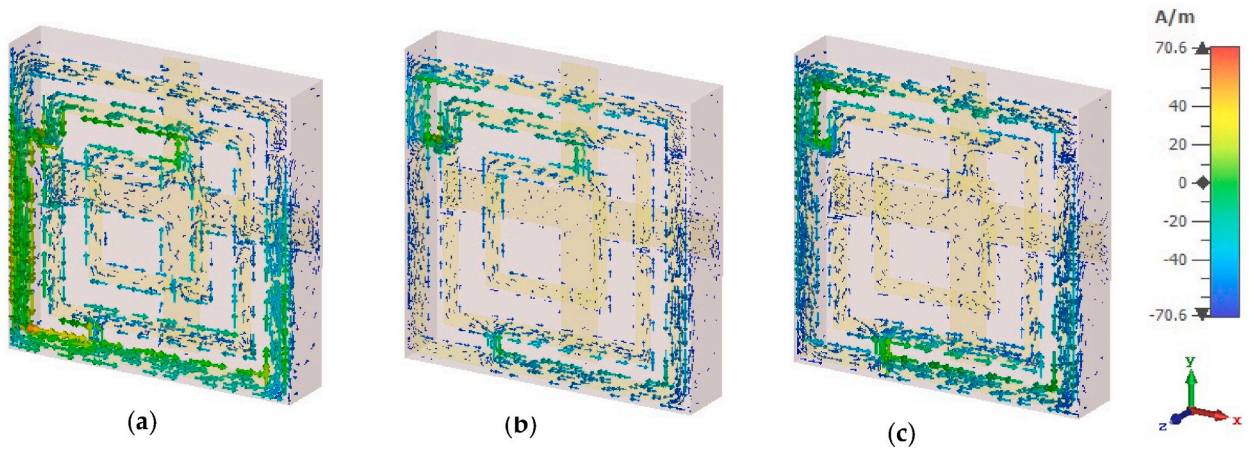


Fig. 8. Surface current distributions at resonance frequency: (a) 2.75 GHz; (b) 5.2 GHz; and (c) 6.3 GHz.

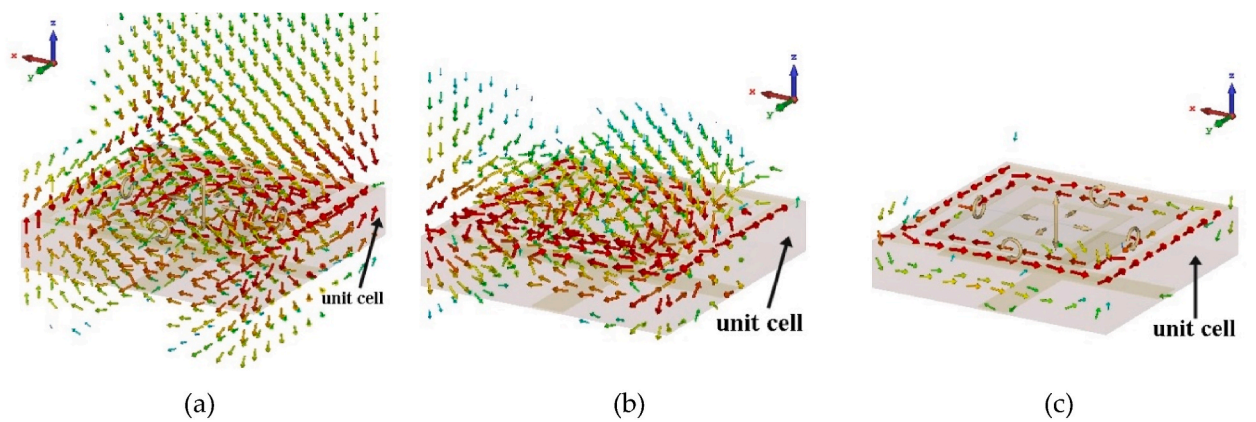







Fig. 9. Poynting vector distributions at the resonance frequencies (a) 2.75 GHz, (b) 5.2 GHz, and (c) 6.3 GHz.

Table 3
TSRCSR metamaterial design evaluation from initial to final state with parameters.

Design states					
Metamaterial	Design 1	Design 2	Design 3	Design 4	Design 5
Peak Points (GHz)	3.54	3.55, 5.48	3.55, 5.45	3.31, 3.54, 7.18	2.75, 5.2, 6.3
Magnitude in dB	-44.77	-42.42, -21.11	-43.11, -20.15	-23.85, -39.37, -30.57	-25.51, -25.58, -32.39
Bandwidth in GHz (<-10 dB)	3.22 – 3.8	3.25 – 3.78, 5.45 – 5.52	3.24 – 3.78, 5.42 – 5.48	3.21 – 3.35, 3.39 – 3.71, 7.03 – 7.27	2.73-2.81, 5.1-5.26, 6.04 – 6.4

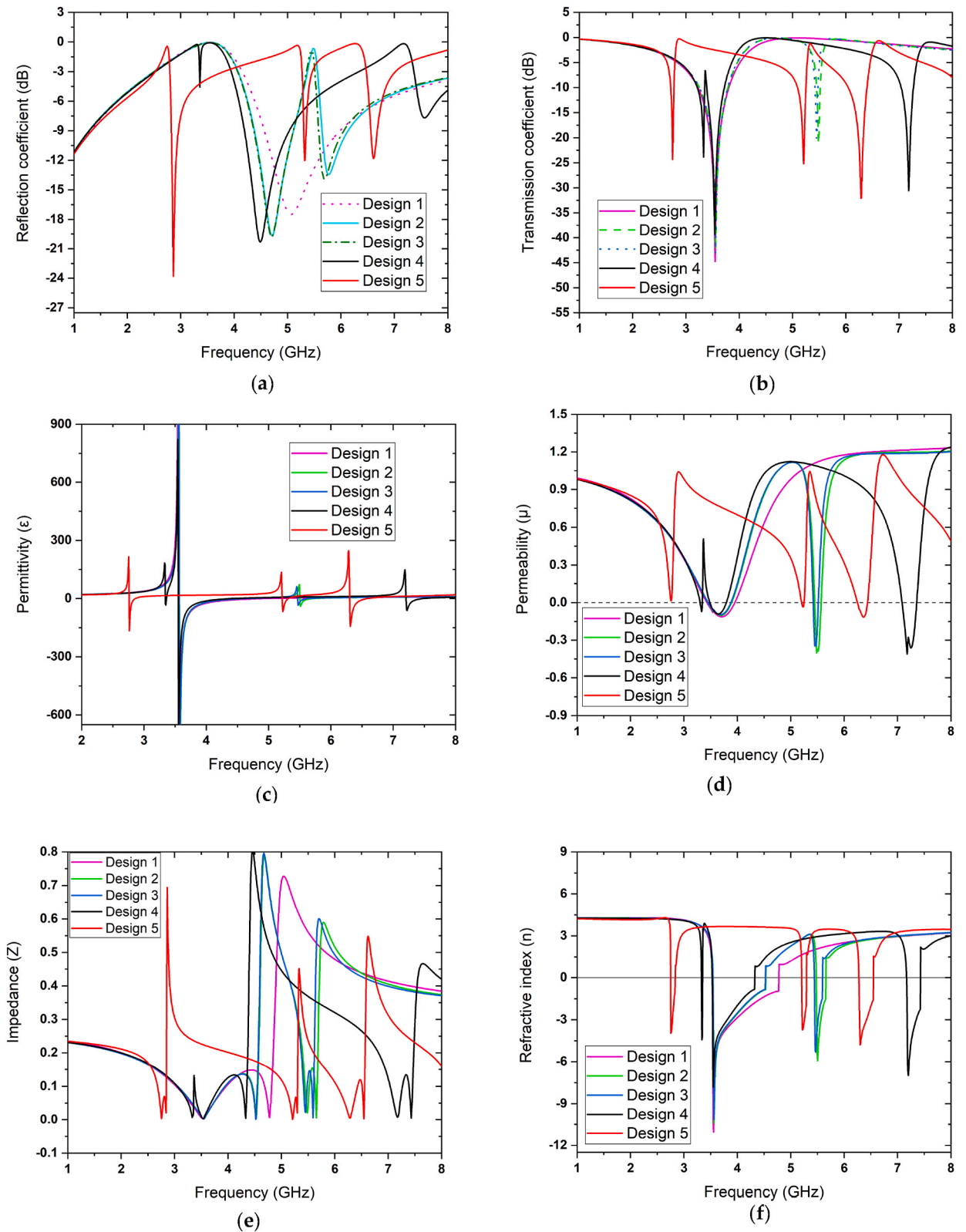


Fig. 10. Metamaterial design evolution of: (a) reflection coefficient; (b) transmission coefficient; (c) real part of relative permittivity; (d) real part of relative permeability; (e) impedance; and (f) refractive index.

represents the graphs to confirm that, the proposed metamaterial design has efficient characteristics in every property, found as a double negative (DNG) metamaterial. Fig. 10a and b show the scattering parameters where it is observed that the proposed metamaterial design achieves the required resonances and the bandwidths are observed below -10 dB. Fig. 10c displays the permittivity where the negative permittivity is found within certain frequency ranges. It is essential to investigate several unit cell layouts to choose the one that offers the requisite negative permittivity properties. It is possible to strengthen the negative permittivity effect by utilizing multilayer metamaterial constructions. The unit cell design has been adjusted following the frequency ranges where negative permittivity is more effective. Fig. 10d indicates the ability to control the magnetic properties of materials through negative permeability. Metamaterials open up a wide range of innovative applications that were not possible with conventional materials. By tailoring the magnetic properties of metamaterials, the design can be made more efficient, with improved radiation characteristics, bandwidth, gain and directivity [38]. Fig. 10e depicts the impedance of the metamaterial unit cell where the near-zero impedance is found, implying that the real part approaches zero while the imaginary part remains significant at central frequencies. When the real part of the impedance is close to zero, electromagnetic waves experience a unique refractive behaviour, leading to negative refraction. Fig. 10f illustrates the negative refractive index of the proposed metamaterial that establishes the proposed design can be used as a perfect metamaterial with its extraordinary characteristics at certain frequencies.

5.2. Split gap and perimeter modification

When subjected to an external magnetic field, the adopted square-shaped ring resonator allows current to flow from one ring to another via the inter-rings gap. It also features a more pronounced current distribution and a slower resonance frequency. It also has an additional capacitive connection to the composite structure, which allows for more robust resonant behaviour. On the other hand, the length and split gap of SRR become the important properties. The adjustments of these elements also impact the capacitance and inductance. The modification of the split gaps has an impact on the resonance frequencies. The split gap in SRR significantly impacts the suggested unit cell. Variations in capacitance value affect unit cell resonance because of the connection between capacitance and resonance frequency. The split gap g_4 on the proposed unit cell is illustrated in this study for understanding the evaluation of the resonant result. We have explored the frequency variations in response to split gap width modifications.

Fig. 11 a represents the transmission coefficients without the split gaps. Fig. 11 b demonstrates the length of the split gap is tweaked in the design until the required result is achieved. It is also investigated when there is no split gap and the split gap is introduced within the range of 0.2–1.4 mm. Whenever there are no split gaps, it is observed that Designs 1 to 4 have the almost same single resonance. Though in Design 2 another SRR and Design 3, two SRRs are added a resonance peak is observed near 7.15 GHz along with three design structures. It shows another resonance response when the connection is made between the SRRs. The new resonance is seen near at 5.2 GHz. We investigated introducing different width split gaps on the inner SRR where modifying the width, there is resonance frequency shifting is observed near 5.2 GHz. Fig. 11 demonstrates the transmission coefficients of the unit cell design with split gaps without modifying split gaps.

5.3. Polarization insensitivity

Fig. 12 displays co-polarized and cross-polarized reflection coefficients when the incident fields are x and y polarized. It is observed that the cross-polarized transmission is large compared with the co-polarized reflection in the operating resonances. Moreover, the cross-polarized transmission coefficient is stable at different incidence angles. Throughout the investigation, several angles in stages of

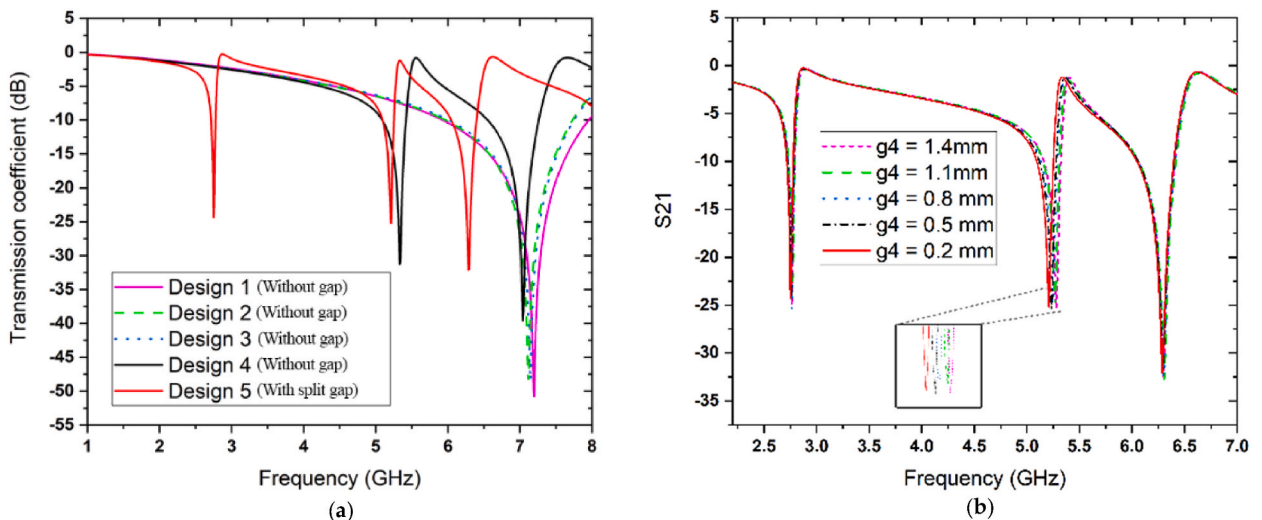


Fig. 11. Metamaterial unit cell transmission coefficient based on (a) without and with split gaps and (b) perimeter modification.

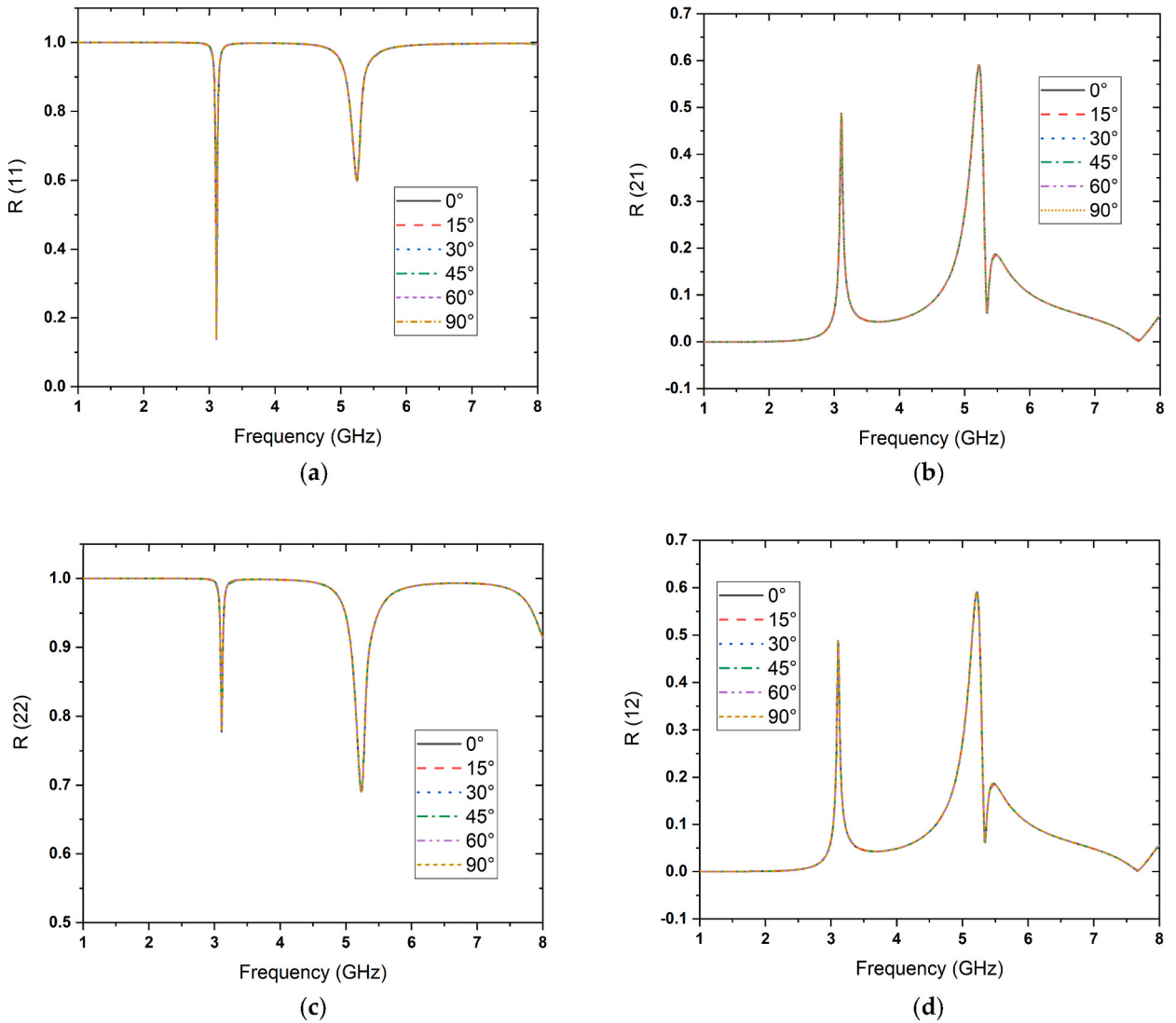


Fig. 12. Co-polarized and cross-polarized reflection and transmission coefficients for different incidence angles: (a) x-polarized incident field (co-polarized); (b) x-polarized incident field (cross-polarized); (c) y-polarized incident field (co-polarized); and (d) y-polarized incident field (cross-polarized).

0° – 90° are used. From the observation, it revealed that the x-polarized incident field (cross-polarized) and y-polarized incident field (cross-polarized) exhibit similar responses. Meanwhile, the x-polarized incident field (co-polarized) and y-polarized incident field (co-polarized) analysis shows slightly different resonance frequencies with varied magnitude values. Co-polarized reflection occurs when the incident and reflected waves have the same polarization. In this article, the co-polarized reflection is not stable, this can happen due to the metamaterial's unique properties, which may result in complex interference patterns and phase relationships. Depending on the specific orientation of the incident wave's polarization and the design of the metamaterial, the response can vary. At the same time, Cross-polarized transmission refers to the phenomenon where an incident electromagnetic wave's electric field (E-field) is oscillating in one direction. (vertically polarized), but the transmitted wave's E-field oscillates in a different direction (horizontally polarized). The parameters of S12 and S21 values remain consistent, indicating a reliable transmission of power and polarization transformation from one port to another.

5.4. Array analysis

This section examines two different-sized array characteristics. Several array configurations have been offered to review the impacts of unit cell coupling. Nearly comparable resonances for the relevant reflection and transmission coefficients are obtained for the metamaterial arrays. Fig. 13 displays the metamaterial arrays and their boundary conditions with the S parameters. The phase difference on the arrays is also observed. The coupling effect allowed the 2×2 and 4×4 sized arrays to attain about a small area of

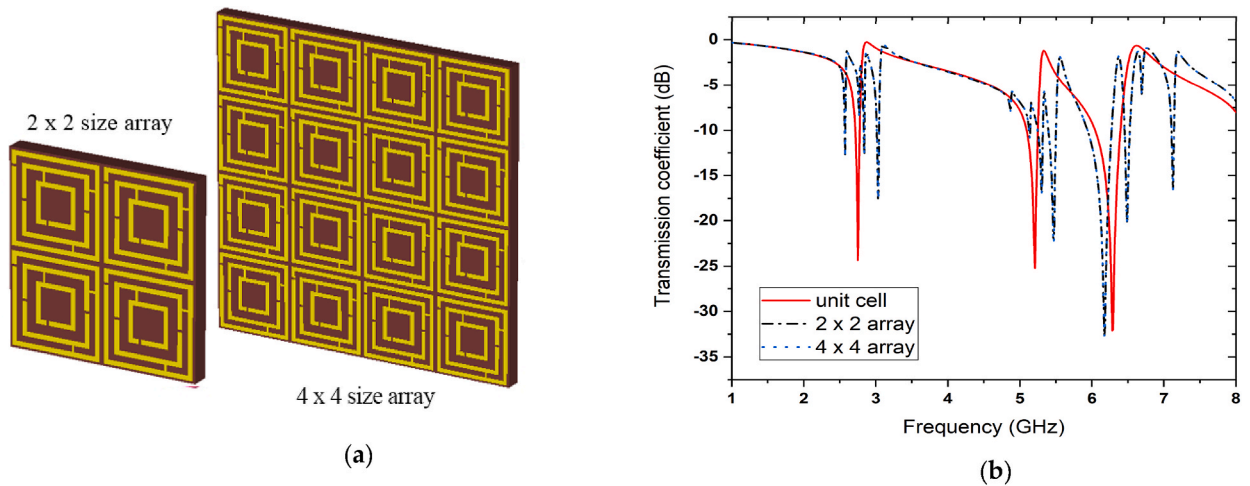


Fig. 13. Metamaterial arrays: (a) 2 × 2 and 4 × 4 sized array; (b) transmission coefficients (S21).

scattered resonance.

Table 4 compares a few recent studies with the proposed unit cell. It demonstrates that smaller width and resonance peaks are frequently found in unit cells with the greatest EMRs. This study’s [26] usage of a smaller unit cell at reduced peak points of 4.3 GHz was recognized. The investigation also found that at 2.38 GHz, a larger design than the previous standard was used [27]. In comparison to these references, the smaller unit cell has a greater EMR. A higher EMR might be reached at a higher resonance peak rather than a smaller unit cell. The effective EMR for the ASR-based metamaterial was 12.78 according to reference [21]. The proposed ASR and WLAN-based metamaterial unit cell indicates an EMR over 13.9. Moreover, the ASR, WLAN, and satellite-based application areas are appropriate for the suggested metamaterial structure. There is scope for extended investigation about modification of the design to achieve optimised results using particle swarm optimization (PSO) algorithm with the integration of the finite element method [39] to utilize the design in other applications such as superlenses, and invisibility cloaks. Overall, the proposed double-layer TSRCRSR metamaterial possesses novel properties despite adopting the miniaturization concept and is suitable for practical application since it shows slight discrepancies in S21 values for either analytical or measurement analyses.

6. Conclusion

In this work, equivalent circuit analysis is focused on and compared with results extracted from the CST-MATLAB software. Meanwhile, the numerical analysis was also further validated by adopting the HFSS simulation program and VNA measurement. The peak points of 2.75, 5.2, and 6.3 GHz serve as indicators of the device’s multi-band capabilities. Furthermore, the measurement process manifests minimal discrepancies in S21 results when compared to the numerical values. The device’s high EMR at 2.75 GHz, which is superior to other researched designs, makes it evident that it is new for the specified application sector associated with ASR, WLAN, and satellite. The recommended structure can also be used for long-distance telecommunication communication systems and mobile communication. In summary, a miniaturised double-layer metamaterial was successfully introduced and analyzed for the proposed application field.

Table 4
Recent related investigation with the proposed design.

Reference	Year	Substrate	Shape	Size (mm ² and wavelength)	Frequency (GHz)	EMR	Application field
[27]	2017	FR-4	Double C	12 × 12 0.101 λ × 0.101 λ	3.36, 8.57, 11.57	7.42	Not specified
[28]	2017	FR-4	Delta loop	6 × 6 0.086 λ × 0.086 λ	4.3, 7.6, 9.8	11.5	Filter, wave absorber
[29]	2019	Rogers RT5800	Double L	10 × 10 0.119λ × 0.119 λ	7.69, 8.47, 12.04, 13.14	3.9	Satellite
[30]	2020	Rogers RO4350B	Inverse-epsilon	10 × 10 0.079 λ × 0.079 λ	2.38, 4.55, 9.42	12.61	Satellite, radar
[31]	2020	FR-4	Hook C shape	8 × 8 0.078 λ × 0.078 λ	2.93	12.78	ASR
Proposed	2023	Rogers RT5880	TSRCRSR	8 × 8 0.073 λ × 0.073 λ	2.75, 5.2, 6.3	13.9	ASR, WLAN, Satellite

Data availability

No data was used for the research described in the article.

Additional information

No additional information is available for this paper.

CRediT authorship contribution statement

Rasheduzzaman Sifat: Writing – original draft, Visualization, Validation, Software, Resources, Methodology, Investigation, Formal analysis, Data curation, Conceptualization. **Mohammad Rashed Iqbal Faruque:** Writing – review & editing, Visualization, Validation, Supervision, Project administration, Investigation, Funding acquisition, Conceptualization. **Tayaallen Ramachandran:** Writing – review & editing, Visualization, Validation, Resources, Investigation. **Mardina Abdullah:** Writing – review & editing, Visualization, Validation, Supervision, Investigation. **Mohammad Tariqul Islam:** Writing – review & editing, Visualization, Validation, Supervision, Investigation. **K.S. Al-Mugren:** Writing – review & editing, Visualization, Validation, Investigation, Funding acquisition.

Declaration of competing interest

The authors declare that they have no known competing financial interests or personal relationships that could have appeared to influence the work reported in this paper.

Acknowledgements

The authors thank the research Universiti Grant, Universiti Kebangsaan Malaysia, Geran Universiti Penyelidikan, Code: GUP-2021-074, who helped conduct the research work. Moreover, the authors express their gratitude to Princess Nourah bint Abdulrahman University Researchers Supporting Project number (PNURSP2023R10), Princess Nourah bint Abdulrahman University, Riyadh, Saudi Arabia.

References

- [1] W.C. Gibson, *The Method of Moments in Electromagnetics*, Chapman and Hall/CRC, 2021.
- [2] V.G. Veselago, Electrodynamics of substances with simultaneously negative and, *Usp. Fiz. Nauk* 92 (7) (1967) 517.
- [3] J.B. Pendry, et al., Magnetism from conductors and enhanced nonlinear phenomena, *IEEE Trans. Microw. Theor. Tech.* 47 (11) (1999) 2075–2084.
- [4] A. Sihvola, *Metamaterials in electromagnetics*, *Metamaterials* 1 (1) (2007) 2–11.
- [5] N.I. Zheludev, The road ahead for metamaterials, *Science* 328 (5978) (2010) 582–583.
- [6] S. Walia, et al., Flexible metasurfaces and metamaterials: a review of materials and fabrication processes at micro-and nano-scales, *Appl. Phys. Rev.* 2 (1) (2015), 011303.
- [7] H. Li, et al., Investigation of multiband plasmonic metamaterial perfect absorbers based on graphene ribbons by the phase-coupled method, *Carbon* 141 (2019) 481–487.
- [8] M. Amiri, et al., Wide-angle metamaterial absorber with highly insensitive absorption for TE and TM modes, *Sci. Rep.* 10 (1) (2020) 1–13.
- [9] J. Zhang, S. Yan, G.A. Vandenbosch, Metamaterial-inspired dual-band frequency-reconfigurable antenna with pattern diversity, *Electron. Lett.* 55 (10) (2019) 573–574.
- [10] F. Khajeh-Khalili, M.A. Honarvar, Novel tunable Peace-logo planar metamaterial unit-cell for millimeter-wave applications, *ETRI J.* 40 (3) (2018) 389–395.
- [11] M. Alibakhshikenari, et al., A Comprehensive Survey on Antennas On-Chip Based on Metamaterial, Metasurface, and Substrate Integrated Waveguide Principles for Millimeter-Waves and Terahertz Integrated Circuits and Systems, *IEEE Access*, 2022.
- [12] R. Sifat, et al., Development of double C-shaped left-handed metamaterial for dual-band wi-fi and satellite communication application with high effective medium radio and wide bandwidth, *Crystals* 12 (6) (2022) 836.
- [13] M. Islam, et al., Microwave imaging sensor using compact metamaterial UWB antenna with a high correlation factor, *Materials* 8 (8) (2015) 4631–4651.
- [14] N. Kundtz, D.R. Smith, Extreme-angle broadband metamaterial lens, *Nat. Mater.* 9 (2) (2010) 129–132.
- [15] Z. Liu, et al., Triple plasmon-induced transparency and optical switch desensitized to polarized light based on a mono-layer metamaterial, *Opt Express* 29 (9) (2021) 13949–13959.
- [16] S. Islam, M. Hasan, M.R.I. Faruque, A new metamaterial-based wideband rectangular invisibility cloak, *Appl. Phys. A* 124 (2) (2018) 160.
- [17] T. Ramachandran, et al., Radar cross-section reduction using polarisation-dependent passive metamaterial for satellite communication, *Chin. J. Phys.* 76 (2022) 251–268.
- [18] M. Faruque, M. Islam, M. Ali, A new design of metamaterials for SAR reduction, *Meas. Sci. Rev.* 13 (2) (2013) 70.
- [19] S. Shen, et al., Recent advances in the development of materials for terahertz metamaterial sensing, *Adv. Opt. Mater.* 10 (1) (2022), 2101008.
- [20] E. Ahamed, et al., Enhancement of magnetic field intensity with a left-handed metamaterial tunnel resonator for obstacle sensing, *Chin. J. Phys.* 70 (2021) 91–105.
- [21] J. Qiu, et al., Ultra-wideband perfect reflection and tunneling by all-dielectric metamaterials, *Opt Lett.* 46 (4) (2021) 849–852.
- [22] I.N. Idrus, et al., An oval-square shaped split ring resonator based left-handed metamaterial for satellite communications and radar applications, *Micromachines* 13 (4) (2022) 578.
- [23] S. Al-Bawri, M. Islam, M.J. Singh, Analysis of a tuneable NZRI metamaterial unit cell for satellite applications, in: *IOP Conference Series: Earth and Environmental Science*, IOP Publishing, 2023.
- [24] E. Ahamed, et al., Reconfigurable THz metamaterial filter based on binary response for information processing system, *Front. Physiol.* 9 (661060) (2021).
- [25] R. Xu, et al., Actively logical modulation of MEMS-based terahertz metamaterial, *Photon. Res.* 9 (7) (2021) 1409–1415.
- [26] C. Xu, et al., Reconfigurable Terahertz Metamaterials: from Fundamental Principles to Advanced 6G Applications, *Iscience*, 2022, 103799.
- [27] M.R.I. Faruque, et al., Design and analysis of a new double C-shaped miniaturized metamaterial for multiband applications, *Appl. Phys. A* 123 (5) (2017) 1–8.

- [28] D. Marathe, K. Kulat, A compact triple-band negative permittivity metamaterial for C, X-band applications, *Int. J. Antenn. Propag.* 2017 (2017) 1–12, <https://doi.org/10.1155/2017/7515264>. Article ID: 7515264.
- [29] A.M. Tamim, et al., Split ring resonator loaded horizontally inverse double L-shaped metamaterial for C-, X-and Ku-Band Microwave applications, *Results Phys.* 12 (2019) 2112–2122.
- [30] M.R. Islam, et al., Square enclosed circle split ring resonator enabled epsilon negative (ENG) near zero index (NZI) metamaterial for gain enhancement of multiband satellite and radar antenna applications, *Results Phys.* 19 (2020), 103556.
- [31] R. Sifat, et al., Electric field controlled cohesive symmetric hook-C shape inspired metamaterial for S-band application, *Chin. J. Phys.* 68 (2020) 28–38.
- [32] X. Chen, et al., Robust method to retrieve the constitutive effective parameters of metamaterials, *Phys. Rev.* 70 (1) (2004), 016608.
- [33] S. Arslanagić, et al., A review of the scattering-parameter extraction method with clarification of ambiguity issues in relation to metamaterial homogenization, *IEEE Antennas Propagation Magazine* 55 (2) (2013) 91–106.
- [34] A. Taflov, S.C. Hagness, M. Picket-May, Computational electromagnetics: the finite-difference time-domain method, *The Electrical Engineering Handbook* 3 (2005) 629–670.
- [35] M.B. Hossain, et al., Modified double dumbbell-shaped split-ring resonator-based negative permittivity metamaterial for satellite communications with high effective medium ratio, *Sci. Rep.* 11 (1) (2021), 19331.
- [36] M. Moniruzzaman, et al., Gap coupled symmetric split ring resonator based near zero index ENG metamaterial for gain improvement of monopole antenna, *Sci. Rep.* 12 (1) (2022) 1–22.
- [37] Z. Fang, J. Zhan, Deep physical informed neural networks for metamaterial design, *IEEE Access* 8 (2019) 24506–24513.
- [38] F. Khajeh-Khalili, et al., Gain enhancement and mutual coupling reduction of multiple-input multiple-output antenna for millimeter-wave applications using two types of novel metamaterial structures, *Int. J. RF Microw. Computer-Aided Eng.* 30 (1) (2020), e22006.
- [39] N. Di Cesare, D. Chamoret, M. Domaszewski, Optimum topological design of negative permeability dielectric metamaterial using a new binary particle swarm algorithm, *Adv. Eng. Software* 101 (2016) 149–159.